

## Supplementary information: Polaron-driven surface reconstructions

Michele Reticcioli,<sup>1</sup> Martin Setvin,<sup>2,\*</sup> Xianfeng Hao,<sup>1,3</sup> Peter Flauger,<sup>1</sup>  
Georg Kresse,<sup>1</sup> Michael Schmid,<sup>2</sup> Ulrike Diebold,<sup>2</sup> and Cesare Franchini<sup>1,†</sup>

<sup>1</sup>*University of Vienna, Faculty of Physics and Center for Computational Materials Science,  
Sensengasse 8/12, A-1090 Vienna, Austria*

<sup>2</sup>*Institute of Applied Physics, Vienna University of Technology,  
Wiedner Hauptstrasse 8-10/134, 1040 Vienna, Austria*

<sup>3</sup>*Key Laboratory of Applied Chemistry,  
Yanshan University, Qinhuangdao 066004, P. R. China*

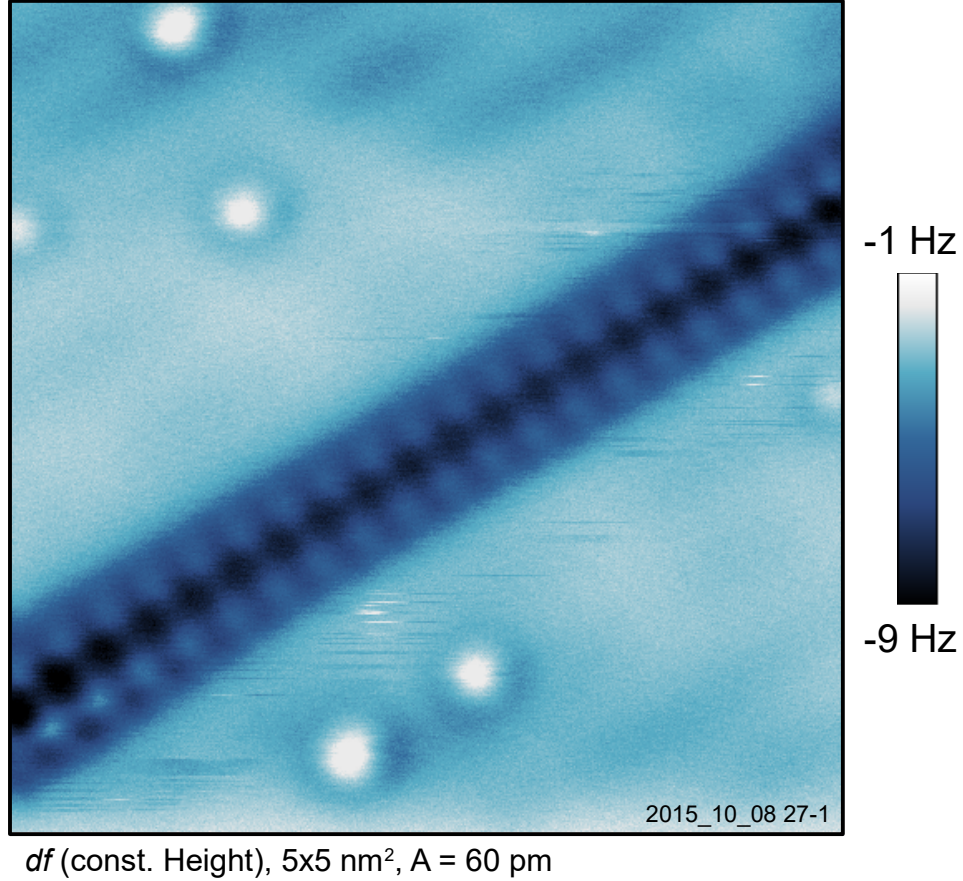


FIG. S1. **The  $(1 \times 2)$  reconstruction imaged by a CO-terminated tip.** The bright spots in the surrounding region are single CO molecules adsorbed at the  $(1 \times 1)$  phase.

## I. DIFFERENT TIP TERMINATIONS AND AFM CONTRAST

In order to obtain well-defined atomic resolution in AFM images, we purposely functionalized the tip in two different ways: By an O atom and by a CO molecule. The images presented in Fig. 1 of the main text were measured with an O-terminated tip. For comparison, an image measured with a CO-terminated tip is shown in Fig. S1. With the CO-termination we could resolve the  $(1 \times 2)$  reconstruction and obtain similar images as with the O-terminated tips. However, the CO-termination did not provide good results on the  $(1 \times 1)$  phase because the attractive interaction with the surface  $\text{Ti}_{5c}$  atoms was too strong and resulted in losing the CO-functionalization. Both the O-terminated and CO-terminated tips allow imaging the surface oxygen atoms in the repulsive regime with excellent lateral resolution. Best images were obtained with tips, which had negligible attractive force towards the surface

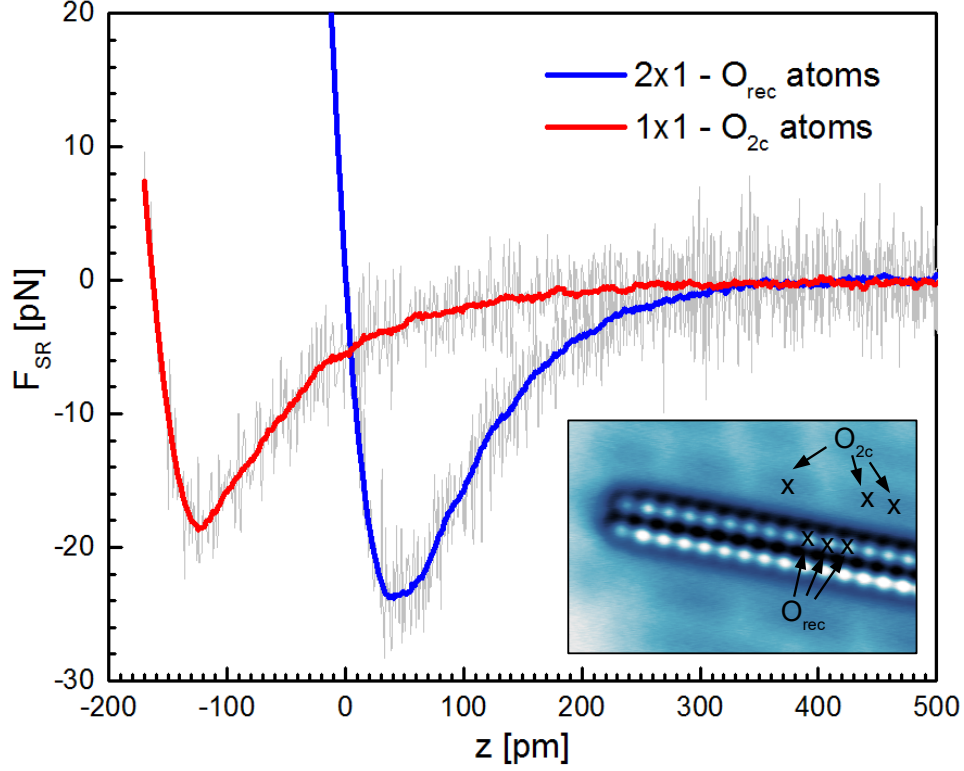


FIG. S2. Short-range chemical forces measured (with a typical tip termination) above the surface O atoms of the  $(1\times 1)$  and  $(1\times 2)$  phases.

$O_{2c}$  atoms - see Fig. S2. The attractive force was only on the order of 20 pN, followed directly by repulsion. Comparison with published calculations of AFM images<sup>1,2</sup> indicates that such tips are terminated by a single O atom in an adatom configuration. The  $F(z)$  curves plotted in Fig. S2 have the long-range contribution subtracted<sup>3</sup> and the Sader formula<sup>4</sup> was used for converting the frequency shift into force.

## II. BUCKLING IN $Ti_2O_3$

### A. Experiment

We found that the  $(1\times 2)$  reconstruction shows two distinctly different appearances in STM images - see Fig. S3. Fig. S3(a) shows a large-area image of the rutile (110) surface, with stripes of the  $(1\times 2)$  reconstruction. Some of the  $(1\times 2)$  stripes are brighter (marked by solid white arrows), and others are darker (marked by dashed white arrows). In many points we

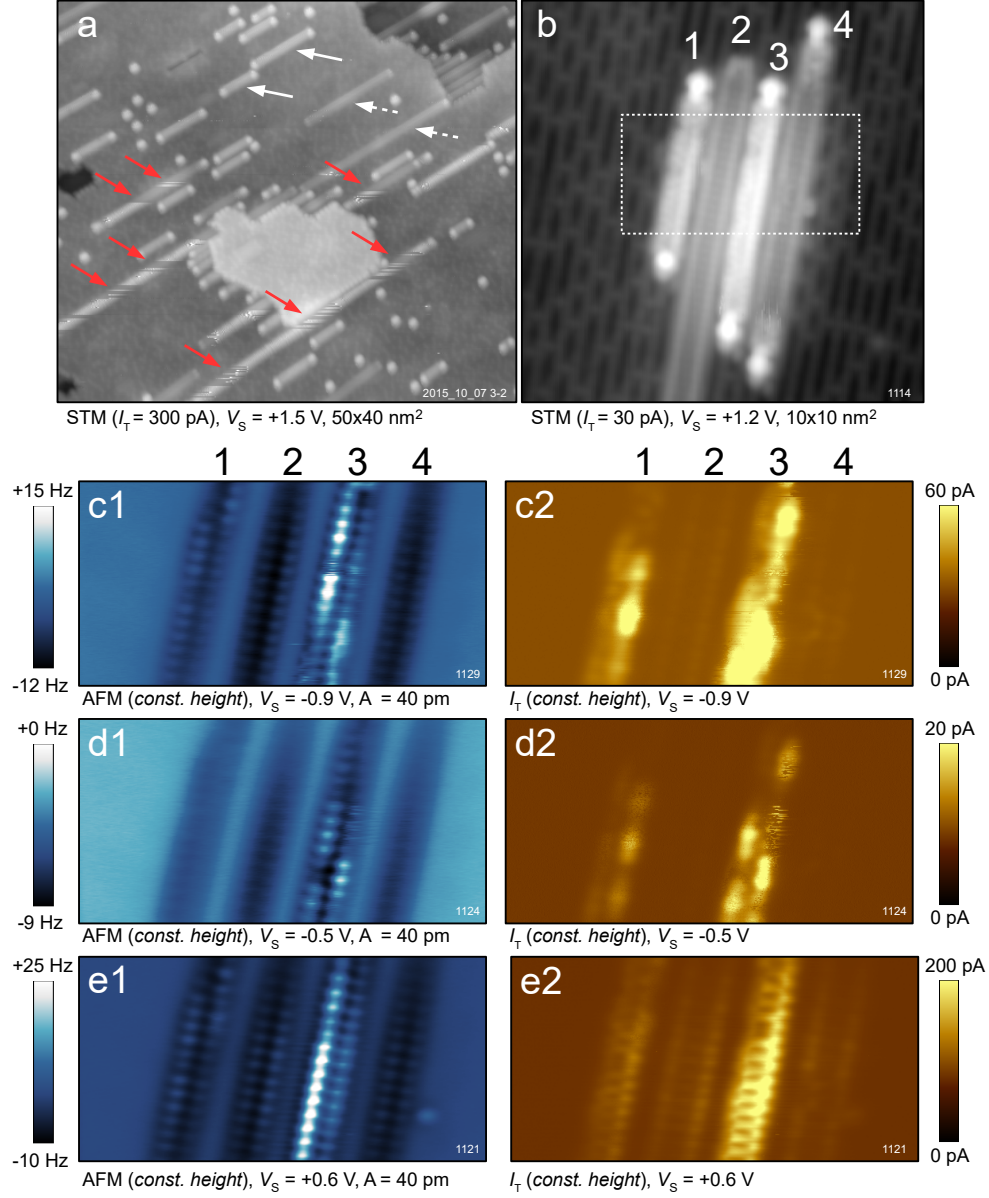


FIG. S3. **Relation between the buckling and STM imaging of the (1 $\times$ 2) reconstruction.** (a), A large-area STM image of a strongly reduced rutile (110) surface. There are brighter and less bright stripes of the (1 $\times$ 2) reconstruction, marked by solid and dashed white arrows. Red arrows mark tip-induced switching between these two configurations. (b), A region with four adjacent stripes of the (1 $\times$ 2) reconstruction. The stripes are labeled by numbers 1 to 4. (c-e), Simultaneous AFM (c1-e1) and STM (c2-e2) images of the selected region, measured in the constant-height mode.

can observe switching between the brighter and darker contrast (marked by red arrows). The switching is tip-induced, and depends both on the sample bias and the tunneling current.

Based on combined STM/AFM imaging we conclude that both the brighter and darker stripes have the same atomic structure, and the STM contrast-switch is related to the row

buckling. In order to illustrate this, we chose an area marked by a dashed rectangle in Fig. S3(b). The inset is imaged in Figs. S3(c-e) at different conditions. There are four ( $1 \times 2$ ) stripes, labeled by numbers (1 to 4). The detailed AFM images in c1-e1 reveal that the lines 1 and 3 are buckled, while lines 2 and 4 are almost symmetric. The different AFM contrasts in c,d,e stems from a varying tip-sample distance. The buckling of line 3 was switched between images d1 and e1, and the buckling switch stems from changing the sample bias polarity. The buckling is stable when the surface is imaged by AFM at zero sample bias, even when imaged in the repulsive regime (the chemical force between the tip and the sample is very small – see Fig. S2). On the other hand, we often observed tip-induced buckling switches induced by tunneling current and applied bias.

By systematic comparison of AFM and STM images, we conclude that the STM signal from the ( $1 \times 2$ ) reconstruction originates from different atoms in the buckled and non-buckled cases. For the buckled chains, the tunneling current is mainly from the surface  $O_{rec}$  and  $Ti_{rec}$  atoms; the stripes 1 and 3 in Fig. S3 are a bit narrower in both filled and empty states. In contrast to this, the non-buckled stripes are a bit broader in both filled- and empty-states STM images. The empty-states maxima fit with the positions of the reconstruction  $O_{3c}$  atoms, while the filled-states are centered on the  $Ti_{S0}^{\alpha}$  and  $Ti_{S0}^{\beta}$  atoms of the surface layer below the reconstruction.

## B. Calculations

Our FPMD calculations for the  $Ti_2O_3$  reconstructed surface show that the  $Ti^{3+}$  atoms prefer to occupy mostly  $Ti_{S0}^{\alpha}$  and  $Ti_{S0}^{\beta}$  sites, as shown in Fig. S4(c). This configuration (with no  $Ti^{3+}$  polarons in the reconstructed row  $Ti_{rec}$  sites) is the most favorable, according to the DFT calculations at  $T = 0$  K. The calculated  $Ti^{3+}$  polaron positions closely resemble the STM images obtained on the non-buckled  $Ti_2O_3$  stripes - see Fig. S4(a) and S4(b). Even though the polaron positions match well with the experimental STM image, we did not obtain a perfect match with the calculated STM image: In the calculations, the polaron density of states typically hybridizes with the atoms of the reconstructed rows, and the calculated STM images consequently show the top-layer atom positions, which are slightly shifted compared to the experimental data. This shift could be due to the limitation of the

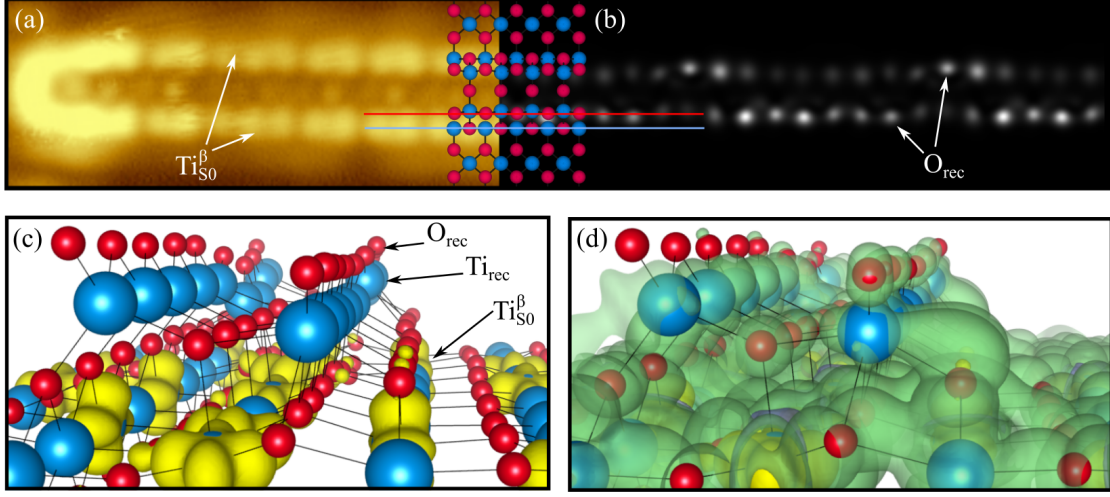


FIG. S4. **Mid-gap states in  $\text{Ti}_2\text{O}_3$ .** (a), Experimental occupied-states STM image for a  $\text{Ti}_2\text{O}_3$  row, which appeared almost symmetric in AFM. (b), Simulated occupied-states STM image corresponding to the lowest energy configuration from the FPMD run. The top-view of the  $\text{Ti}_2\text{O}_3$  model in the inset in panel a and b compares the positions of the bright spots in the experimental and calculated STM images. (c), Detail of the corresponding charge density isosurfaces in  $\text{Ti}_2\text{O}_3$ , showing that polarons are localized at the  $S_0$  layer level. (d), Same as panel c, but for a lower isosurface density.

Tersoff-Hamann approach in which the tip-sample interaction is neglected.

Furthermore, in our FPMD run, the polarons occasionally hop to the  $\text{Ti}_{rec}$  sites. In fact, on average 6% of the total polaronic charge is located at these sites during the FPMD run. In Fig. S5(a) we show the mid-gap charge density for the buckled  $\text{Ti}_2\text{O}_3$  surface with polarons in one  $\text{Ti}_{rec}$  site per reconstructed row. The corresponding mid-gap STM image is shown in Fig. S5(b): the brightest and broadest spots are related to the polarons in the  $\text{Ti}_{rec}$  sites, while, the remaining visible charge comes from the hybridization between polarons at  $S_0$  and  $\text{O}_{rec}$  atoms. The presence of polarons in the  $\text{Ti}_2\text{O}_3$  rows results in stronger buckling, and indeed, the calculated STM images for this configuration closely resembles the experimental results [see the comparison in Fig. S5(c)].

### III. POLARONIC CONFIGURATIONS

The total energy of the  $\text{TiO}_2$  surface at a given  $V_0$  concentration strongly depends on the particular configuration assumed by the small polarons (i.e. polaron distribution in space).



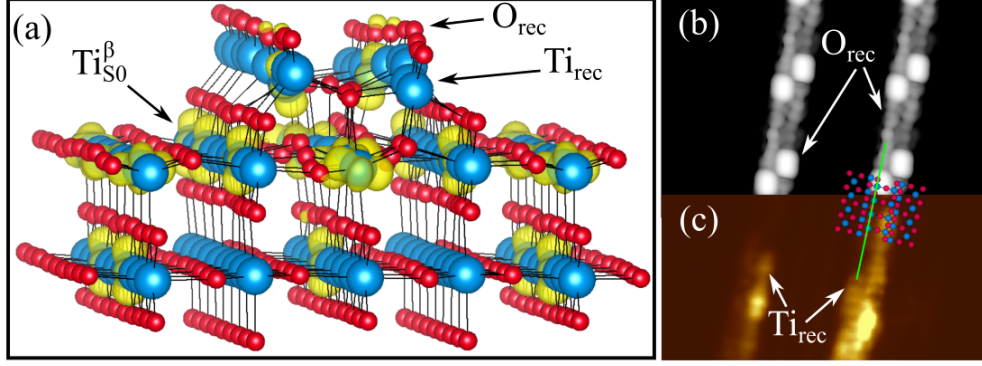


FIG. S5. **Polarons in  $\text{Ti}_{rec}$  sites.** (a), Isosurface model of a configuration obtained during the FPMD run, presenting polarons in  $\text{Ti}_{rec}$  sites. (b), Simulated mid-gap state STM image for the same structure. (c), Experimental filled state STM image compared via the top-view of the  $\text{Ti}_2\text{O}_3$  model in the inset to the simulated STM image for the mid-gap states.

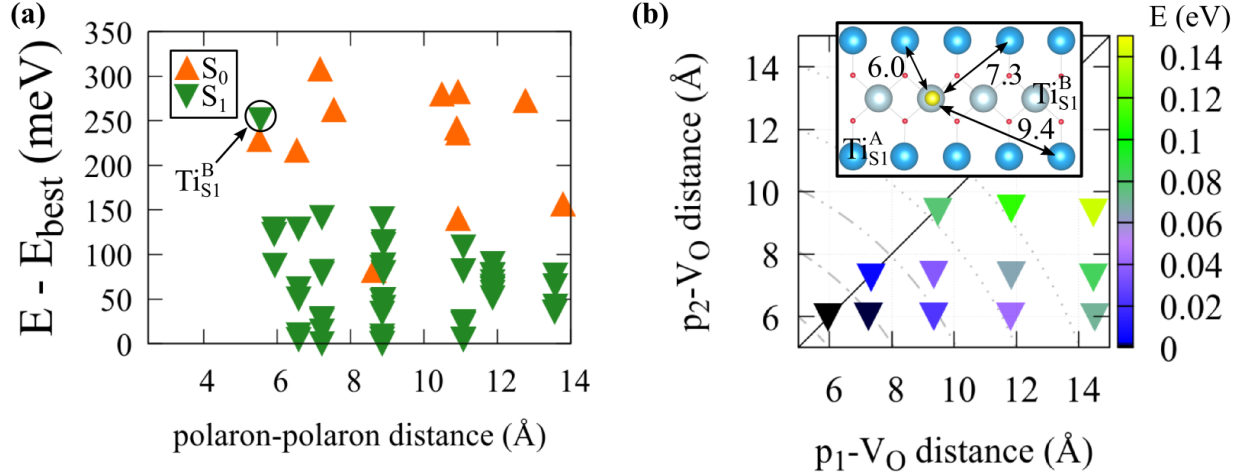


FIG. S6. **Polaronic configurations at  $c_{\text{V}_\text{O}} = 5.6\%$  (1  $\text{V}_\text{O}$  in the  $9 \times 2$  cell).** (a), Energy of the various configurations explored in the FPMD shown with respect to the polaron-polaron distance. Configurations with at least one polaron in  $\text{S}_0$  and both polarons in the  $\text{S}_1$  layer are represented by up-pointing and down-pointing triangles, respectively. The circle represents the configuration with a polaron in a  $\text{Ti}_{\text{S}_1}^\text{B}$  site. (b), Energy of the lowest-energy configurations in the FPMD, with both polarons in  $\text{Ti}_{\text{S}_1}^\text{A}$  sites, shown as color gradient with respect to the distances of the  $p_1$  and  $p_2$  polarons from the  $\text{V}_\text{O}$  site. The inset shows the distances between the  $\text{V}_\text{O}$  and the  $\text{Ti}_{\text{S}_1}^\text{A}$  sites.

Therefore, we have explored and compared several polaronic configurations for every  $\text{V}_\text{O}$  concentration under investigation. The configurations considered were obtained by means of FPMD calculations at  $T = 700$  K, as a result of the thermal activated hopping of the polarons. The respective total energies have been calculated by relaxing each inequivalent configuration at  $T=0$  K.

In Fig. S6 we show the analysis of the energy stability for the various configurations at

$c_{V_O} = 5.6\%$ , i.e. one oxygen vacancy in the  $9 \times 2$  cell, which leads to the formation of two polarons. Overall, as shown in Fig. S6(a), configurations with both polarons in  $Ti_{S1}^A$  sites (up-pointing triangles) result in more favorable energies compared to cases with at least one polaron in a  $Ti_{S0}^A$  site (down-pointing triangles). Particular configurations with at least one S0 polaron show energy values comparable to most configurations with both polarons in the  $Ti_{S1}^A$  sites. One of these particularly favorable S0-S1 configurations was found to be the most stable one in a previous work<sup>5</sup>, while other researchers<sup>6-8</sup> proposed that the most stable configuration involves both polarons in the S1 layer, occupying  $Ti_{S1}^A$  sites, in agreement with our analysis. The formation of a polaron in a  $Ti_{S1}^B$  site [circle in Fig. S6(a)] worsens the energy as compared to the  $Ti_{S1}^A$  sites. Considerable energy differences are also due to the relative position of one polaron with respect to the position of the second polaron. In fact, during the  $c_{V_O} = 5.6\%$  FPMD run, polarons are never found at two adjacent Ti-sites (about  $3\text{\AA}$ ) due to the strong polaron-polaron repulsion [as evident from Fig. S6(a)].

Minor corrections to the energy are related to the polaron-vacancy interaction. In Fig. S6(b) we show the total energy of the most favorable configurations with polarons in  $Ti_{S1}^A$  sites with respect to the distance from the oxygen vacancy. In the most stable configuration both polarons sit in  $Ti_{S1}^A$  sites adjacent to the  $V_O$  (as shown in Fig. 2a in the main text). The energy increases progressively with increasing polaron-vacancy distance, i.e. the  $V_O$ 's result as attraction centers for the polarons. Therefore, as mentioned in the main text, the total energy of a  $Ti_{S1}^A$ -polaronic configuration mostly depends on the polaron-polaron repulsion, and it is perturbed by the polaron- $V_O$  attraction.

#### IV. $V_O$ DISTRIBUTION AT THE SURFACE

In our calculations we have used a model where the vacancies are distributed equidistant to mimic the experimental situation, as explained and justified below.

The oxygen vacancies are nominally positively charged, and exhibit a repulsive interaction. This repulsion can be estimated both theoretically and experimentally - see Fig. S7. Panel (a) shows the calculated contribution of the  $V_O$  distribution to the total energy of the slab, decoupled from the polaron- $V_O$  contribution (this is done by performing non-spin polarized calculations, which do not allow for polaron trapping). Here we show the results obtained



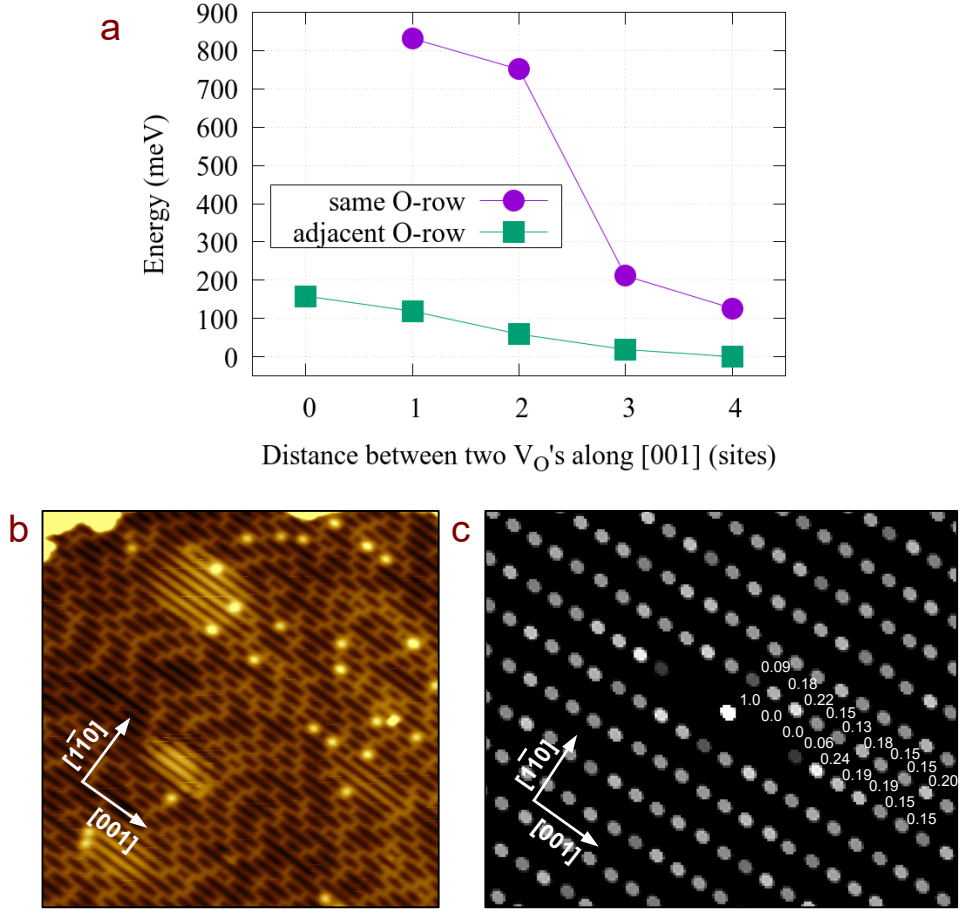


FIG. S7. **Oxygen vacancy distribution.** (a), Calculated total energy of the (9×2) surface slab with two oxygen vacancies (*i.e.*  $c_{VO} = 11.1\%$ ). The oxygen vacancies are placed at different sites in the same or in adjacent  $O_{2c}$  rows. To avoid the additional complication of  $V_O$ -polaron interactions, polaron formation is here inhibited by performing non spin-polarized calculations. (b), Experimental STM image of a surface with  $\approx 15\%$   $V_O$ , used for calculating the  $V_O$  autocorrelation function. (c) Experimental autocorrelation function of the  $V_O$  positions. A few bright  $V_O$ -free areas are attributed to subsurface argon bubbles left over from sputtering. The numbers denote values of the autocorrelation for selected points.

for the unreconstructed surface with two  $V_O$ 's ( $c_{VO} = 11.1\%$ ) placed at different sites. The calculated results are compared with the autocorrelation function (Fig. S7(c), calculated in a similar way to ref. 9) extracted from the experimental image displayed in panel (b). Both, theoretical and experimental data indicate a strong repulsion between  $V_O$ 's along the [001] direction, and a significantly weaker repulsion along the [1-10] direction. Specifically, the two nearest neighbor positions along the [001] directions are forbidden, and there is still a strong repulsion on the third nearest neighbor site. In the perpendicular direction, there is a visible

repulsion only for the first nearest neighbor. As a result, the experimental AFM and STM images, show a clear tendency of the  $(1\times 1)$  phase to stabilize a homogeneous distribution of  $V_O$ 's. Consistently with these considerations, we distributed the  $V_O$ 's homogeneously (maximizing  $V_O$ - $V_O$  distances) in our model slabs.

Clearly, using "nonphysical" (e.g. unfavorable)  $V_O$  distributions would change the polaron energetics in the MD runs, and would affect the overall phase diagram as well as the  $(1\times 1)$  to  $(1\times 2)$  transition.

## V. THE $U$ PARAMETER

Density functional theory allows for formation of polarons only for values of the on-site repulsion  $U$  beyond a critical threshold. In the bulk of rutile  $TiO_2$  (without  $V_O$ ) the value of the effective  $U$  on the Ti  $d$ -states was found to be 3.9 eV by using the constrained random phase approximation (cRPA)<sup>10</sup>. As discussed already in the Methods section, we adopted this value of  $U$  to perform our calculations in order to describe the role of polarons in the  $(1\times 1)$  to  $(1\times 2)$  surface phase transition. This  $U = U^{cRPA}$  favors the formation of polarons with respect to the delocalized electrons both in the bulk and on the surface of rutile, and explain the  $(1\times 1)$  to  $(1\times 2)$  transition, as discussed in the main text.

However, to check the robustness of our conclusions and conclusions against the value of  $U$  we have tested other values of  $U$ . Our results, shown in Fig. S8 show that our interpretation is valid for a wide range of  $U$  values, even for a very small  $U$  of 1.5 eV. Importantly, these data clearly indicate that the  $1\times 2$  reconstruction favors polaron formation more than the  $1\times 1$  phase at high  $V_O$  concentration, as the reconstruction provides larger polaronic energy at any value of  $U$ .

Specifically, in Fig. S8(a) we show the behavior of the polaron formation energy  $E_{POL}$  as function of the chosen  $U$ , for the stable structures obtained by using  $U = U^{cRPA} = 3.9$  eV (see Methods section). The gain in energy in the  $(1\times 2)$  reconstruction with respect to the reduced  $(1\times 1)$  surfaces results to be only slightly dependent on the  $U$  (*i.e.* the various  $E_{POL}(U)$  lines are essentially parallel). Furthermore, near-surface polarons remain localized (*i.e.*  $E_{POL} < 0$ ) even at very low values of  $U$  (up to  $\simeq 2.3$  eV) at the optimal concentration of

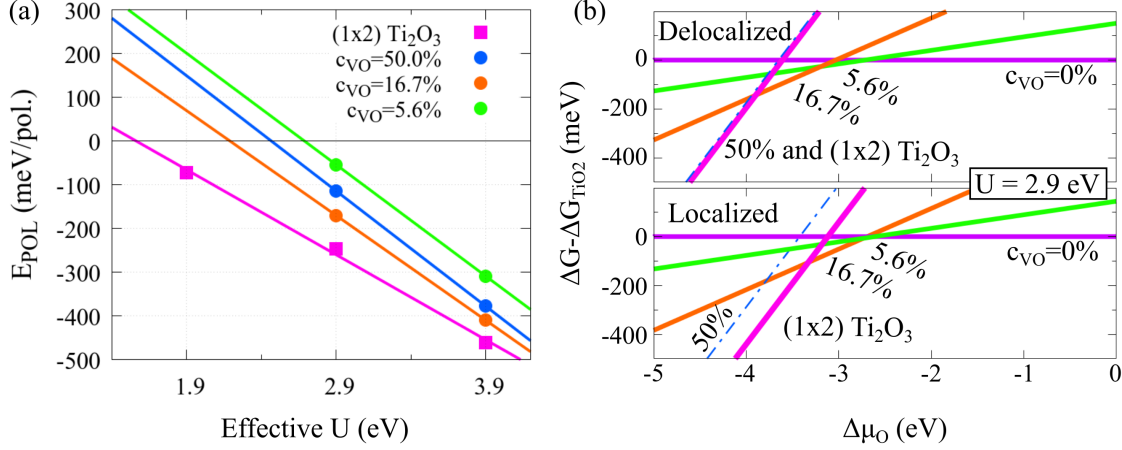


FIG. S8. **Effect of the  $U$  parameter.** (a), Polaron formation energy  $E_{\text{POL}}$  calculated as in Eq. 3 in the main text, by using different values of the on-site effective  $U$  parameter. (b)  $\text{TiO}_2(110)$  surface phase diagram; surface free energy  $\Delta G$  (calculated using  $U = 2.9$  eV) for the most stable configurations obtained from the MD (by using  $U = U^{\text{cRPA}} = 3.9$  eV) for the reduced  $(1 \times 1)$  structures at different  $V_{\text{O}}$  concentrations (all lines except pink) and for the  $(1 \times 2)$   $\text{Ti}_2\text{O}_3$  reconstruction (pink line) as a function of the oxygen chemical potential  $\Delta\mu_{\text{O}}$ . The delocalized and localized solutions are presented in the upper and lower panel, respectively. Even at this low value of  $U = 2.9$  eV, electron localization clearly favors the  $(1 \times 2)$  reconstruction.

oxygen vacancies  $c_{\text{VO}} = 16.7\%$ ) and (up to  $\simeq 1.5$  eV) in the reconstructed phase. Moreover, we find that the choice of  $U$  is not crucial in changing the physics of the  $(1 \times 1)$  to  $(1 \times 2)$  transition. In fact, the phase diagram obtained for  $U = 2.9$  eV, shown in Fig. S8(b), is qualitatively analogous to the corresponding one obtained for  $U = U^{\text{cRPA}} = 3.9$  eV (Fig. 4 in the main text), and confirm the polaron-driven character of the transition.

## VI. ELECTRONIC ENERGY

The evolution of the density of states (DOS) as a function of  $V_{\text{O}}$  concentration shown in Figure S9 supports the discussion on the role of the electronic energy  $E_{\text{EL}}$  (and its coupling with the structural energy) elaborated in the main text: at low  $c_{\text{VO}}$  (5.6%) the polarons form a well localized peak below the Fermi energy. By increasing  $c_{\text{VO}}$  the polarons start to populate levels at lower energies, but above  $c_{\text{VO}}=22.2\%$  the peak broadens towards higher energies, which lead to an increase of  $E_{\text{EL}}$  (Fig. 5, main text).

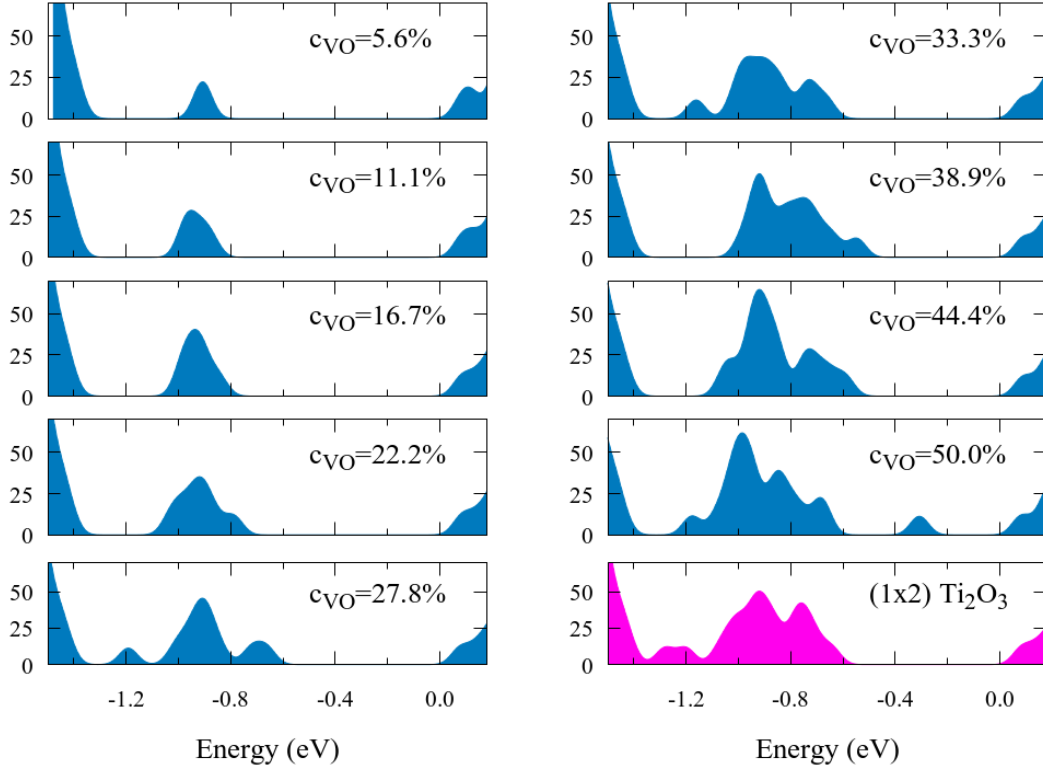


FIG. S9. **Polaronic peak.** Calculated electronic density of states (DOS), given as states/eV, showing the top of the valence band, the polaronic peak and the bottom of the conduction band, in the reduced (1×1) surfaces at various  $V_O$  concentrations and in the (1×2) phase.

---

\* [setvin@iap.tuwien.ac.at](mailto:setvin@iap.tuwien.ac.at)

† [cesare.franchini@univie.ac.at](mailto:cesare.franchini@univie.ac.at)

<sup>1</sup> A. Yurtsever, D. Fernandez-Torre, C. Gonzalez, P. Jelinek, P. Pou, Y. Sugimoto, M. Abe, R. Perez, and S. Morita, “Nc-afm imaging of the  $\text{tio}_2(110)$ -(1×1) surface at low temperature,” *Phys. Rev. B* **85**, 125416 (2012).

<sup>2</sup> R. Bechstein, C. Gonzalez, J. Schutte, P. Jelinek, R. Perez, and A. Kuhnle, ““all-inclusive” imaging of the rutile  $\text{tio}_2(110)$  surface using nc-afm.” *Nanotechnology* **20**, 505703 (2009).

<sup>3</sup> M. A. Lantz, H. J. Hug, R. Hoffmann, P. J. A. van Schendel, P. Kappenberger, S. Martin, A. Baratoff, and H.-J. Güntherodt, “Quantitative measurement of short-range chemical bonding forces,” *Science* **291**, 2580–2583 (2001),

<http://science.sciencemag.org/content/291/5513/2580.full.pdf>.

- <sup>4</sup> John E. Sader and Suzanne P. Jarvis, “Accurate formulas for interaction force and energy in frequency modulation force spectroscopy,” *Applied Physics Letters* **84**, 1801–1803 (2004), <http://aip.scitation.org/doi/pdf/10.1063/1.1667267>.
- <sup>5</sup> Cristiana Di Valentin, Gianfranco Pacchioni, and Annabella Selloni, “Electronic structure of defect states in hydroxylated and reduced rutile  $\text{TiO}_2(110)$  surfaces,” *Phys. Rev. Lett.* **97**, 166803 (2006).
- <sup>6</sup> Piotr M. Kowalski, Matteo Farnesi Camellone, Nisanth N. Nair, Bernd Meyer, and Dominik Marx, “Charge localization dynamics induced by oxygen vacancies on the  $\text{TiO}_2(110)$  surface,” *Phys. Rev. Lett.* **105**, 146405 (2010).
- <sup>7</sup> N. Aaron Deskins, Roger Rousseau, and Michel Dupuis, “Distribution of  $\text{Ti}^{3+}$  surface sites in reduced  $\text{TiO}_2$ ,” *The Journal of Physical Chemistry C* **115**, 7562–7572 (2011), <http://dx.doi.org/10.1021/jp2001139>.
- <sup>8</sup> C. M. Yim, M. B. Watkins, M. J. Wolf, C. L. Pang, K. Hermansson, and G. Thornton, “Engineering polarons at a metal oxide surface,” *Phys. Rev. Lett.* **117**, 116402 (2016).
- <sup>9</sup> Martin Setvin, Maria Buchholz, Weiyi Hou, Cui Zhang, Bernhard Stollger, Jan Hulva, Thomas Simschitz, Xiao Shi, Jiri Pavelec, Gareth Steven Parkinson, MingChun Xu, Yuemin Wang, Michael Schmid, Christof Woell, Annabella Selloni, and Ulrike Diebold, “A multitechnique study of CO adsorption on the  $\text{TiO}_2$  anatase (101) surface,” *J. Phys. Chem. C* **119**, 21044–21052 (2015).
- <sup>10</sup> Martin Setvin, Cesare Franchini, Xianfeng Hao, Michael Schmid, Anderson Janotti, Merzuk Kaltak, Chris G. Van de Walle, Georg Kresse, and Ulrike Diebold, “Direct view at excess electrons in  $\text{TiO}_2$  rutile and anatase,” *Phys. Rev. Lett.* **113**, 086402 (2014).